ISSN 1063-7710, Acoustical Physics, 2018, Vol. 64, No. 6, pp. 760–773. © Pleiades Publishing, Ltd., 2018.
Original Russian Text © V.A. Titarev, G.A. Faranosov, S.A. Chernyshev, A.S. Batrakov, 2018, published in Akusticheskii Zhurnal, 2018, Vol. 64, No. 6, pp. 737–751.

ACOUSTIC ECOLOGY. NOISE AND VIBRATION

Numerical Modeling of the Influence of the Relative Positions of a Propeller and Pylon on Turboprop Aircraft Noise

V. A. Titarev[a, b], G. A. Faranosov[b, c, *], S. A. Chernyshev[b], and A. S. Batrakov[d]

[a] *Federal Research Center "Computer Science and Control", Russian Academy of Sciences, Moscow, 119333 Russia*
[b] *Central Aerohydrodynamic Institute (TsAGI), Moscow Research Complex, Moscow, 107005 Russia*
[c] *Perm National Research Polytechnic University, Perm, 614990 Russia*
[d] *Kazan National Research Technical University n.a. A.N. Tupolev, Kazan, 420111 Russia*
**e-mail: aeroacoustics@tsagi.ru*

Received March 14, 2018

Abstract—The influence of the position of the pylon on the characteristics of propeller noise has been studied as applied to environmental noise calculations for future aircraft. Components related to propeller noise itself and to a signal reflected from a pylon have been separated in the overall noise produced by the propeller–pylon system at the blade passing frequency, and the interference of these signals has been investigated. A numerical method has been developed based on matching of the following two computational blocks: a rotating domain in the immediate vicinity of the propeller and the outer static domain comprising the pylon. A noise calculation procedure by the integral Ffowcs Williams and Hawkings method has been implemented with the use of the Green's function for the convective wave equation.

Keywords: propeller noise, aeroacoustics, numerical simulation, sound signal interference

DOI: 10.1134/S1063771018060118

INTRODUCTION

Propeller noise is an important parameter in the development of turboprop engines for advanced aircraft. Development of low-noise propellers requires highly reliable computational methods for calculating the aeroacoustic characteristics of propellers with the requirement that these methods should not only apply to a stand-alone propeller configuration but also be able to simulate so-called arrangement effects related to possible interaction with nearby airframe elements. In particular, it is of special interest to allow for interaction with a pylon in the two typical configurations of puller and pusher propellers, in which the pylon is downstream and upstream of the propeller, respectively.

The influence of the mutual arrangement of propeller and pylon on the environmental noise produced by the propeller is not as clear as it may seem. On the one hand, it appears that the puller arrangement should be quieter than the pusher one, since a pylon upstream of the propeller creates a turbulent wake incident on the propeller blades, thus causing intensive noise generation, whereas in the case of a pylon downstream of the propeller, the latter operates in a weakly turbulent mode, in this case decreasing the propeller noise. On the other hand, in many advanced aircraft, propellers are expected to be positioned near the tail part of the fuselage, so that the latter and the empennage screen the propeller noise. In this case, the pusher arrangement is used, which has the advantage of allowing flow control devices to be mounted on a pylon (e.g., for flow blowing) that may weaken the turbulent pylon-induced wake and thereby the related amplification of propeller noise. The choice between puller and pusher assemblies thus remains an open problem.

To numerically investigate the effect of a pylon on propeller noise, this study has developed a parallel code for modeling the aerodynamics and acoustics of propellers that allows transient computations, including such complex configurations as propeller–pylon. The method combines the rotating domain near the propeller with the outer static domain that envelops the propeller mounting elements, with the solution interpolated on sliding planes between different mesh domains. An MPI+OpenMP two-level parallel model has been implemented in the software package for supercomputer calculations.

The software was used to study the effect of propeller location (puller or pusher scheme) on propeller-induced tonal sound in the far field. The following two configurations were considered to this end, based on a model six-bladed aircraft propeller: the puller configuration with a pylon in front of the propeller, and the pusher one with the pylon behind the propeller. For each configuration, two-zone spatial computational meshes were created within the rotating domain around the propeller and within the static mesh in the remaining part of the domain, as well as several control surfaces for noise calculations.

A noise calculation procedure by the integral Ffowcs Williams–Hawkings method has been implemented with the use of the Green's function for the convective wave equation; the co-flow is properly taken into account. The noise calculation procedure was verified on a model problem of noise emitted by a dipole harmonic source, with the use of control surfaces characteristic of propeller noise calculations.

Time-accurate transient calculation for the model propeller was used to study the influence of the pylon location (puller and pusher assemblies) on the characteristics of the fundamental harmonic of the propeller noise. Components related to the propeller noise and to the signal scattered by the pylon have been separated in the overall noise produced by the propeller–pylon system, and the interference of these signals has been investigated.

Section 1 describes the developed numerical method for multizone domains; Section 2, the parallel software and computing; Section 3, the studied computational modes and meshes; and Section 4 analyzes the noise results for propeller–pylon configurations in the puller and pusher assemblies. The main results of the work are summarized in the Conclusions.

1. NUMERICAL METHOD FOR MULTIZONE DOMAINS

This section describes the numerical procedure for solving the nonstationary (transient) problem of flow about a complexly shaped helical configuration. The starting point is the earlier created parallel code [1] for modeling the aerodynamics and acoustics of propellers, which solved the problem in its steady-state formulation in a rotating coordinate system. However, such a formulation of the solution procedure does not allow transient calculations or calculations of complex configurations such as the propeller–pylon one. This work resulted in significant refinements to both the numerical procedure and the software package. In the numerical method, a transition was made to modeling that combined a rotating domain (here and below referred to as the "washer") in the immediate vicinity of the propeller and an outer static domain enveloping the pylon. To this end, an implicit numerical method was developed to solve nonstationary problems, including the time-accurate algorithm of interpolation on sliding planes between different mesh domains. The second order of the method is spatially ensured by the common procedure of reconstructing the density, velocity, and pressure using a piecewise-linear function. A three-wave approximate solution to the Riemann problem at cell faces is used to calculate the convective part of the numerical fluxes. Time approximation makes use of the one-step second-order Crank–Nicolson formula and the LU-SGS method to solve equations for the vector increments of conservative variables on an arbitrarily unstructured mesh.

1.1. Design Equations with Allowance for Rotation

In the given problem, the flow region varies in time due to propeller rotation. Numerical simulation therefore requires approaches to constructing with sufficient accuracy a solution to the problem in a moving domain. One such approach is the so-called ALE (arbitrary Lagrangian–Eulerian) formulation (see, e.g., [2, 3]). Within the ALE approach, the classical equations of motion are rewritten with allowance for the motion of the computational domain. The law of motion of the domain can be set arbitrarily. In the case of a rotating propeller, the problem and design equations are simplified, since the computational domain and mesh rotate around one of the coordinate axes as a rigid body without deformation. The motion of the flow region is characterized by the angular velocity vector $\Omega = (\omega_x, \omega_y, \omega_z)^T$, with the motion velocity of an arbitrary spatial point $\mathbf{x} = (x_1, x_2, x_3)$ being

$$\mathbf{V} = (v_1, v_2, v_3)^T = \Omega \times \mathbf{x}.$$

The state of the gas at a physical point in space $\mathbf{x} = (x_1, x_2, x_3)$ at instant t will be characterized by the density ρ, velocity $\mathbf{u} = (u_1, u_2, u_3)$, pressure p, and temperature T. In dimensional vector form, the governing equations with allowance for rotation have the form

$$\frac{\partial}{\partial t}\mathbf{U} + \frac{\partial}{\partial x_k}\mathbf{F}_k^{ALE} = 0, \quad \mathbf{F}_k^{ALE} = \mathbf{F}_k - v_k\mathbf{U}. \tag{1.1}$$

Here $\mathbf{U}$ is the vector of conservative variables and $\mathbf{F}$ is the tensor of convective fluxes along the coordinate directions, i.e.,

$$\mathbf{U} = \begin{pmatrix} \rho \\ \rho u_1 \\ \rho u_2 \\ \rho u_3 \\ E \end{pmatrix}, \quad \mathbf{F}_k = \begin{pmatrix} \rho u_k \\ \rho u_1 u_k + \delta_{1k} p \\ \rho u_2 u_k + \delta_{2k} p, \\ \rho u_3 u_k + \delta_{3k} p \\ (E + p) u_k \end{pmatrix}. \tag{1.2}$$

1.2. Numerical Method of Constructing a Solution in a Single Computational Domain

A numerical solution to the problem is constructed in dimensionless variables that are introduced in the usual way: the values at infinity are selected as the scales of density, temperature, and pressure, etc. As the physical variables $\mathbf{x} = (x_1, x_2, x_3) = (x, y, z)$, let us introduce a computational mesh consisting of cells Vol_i. Each of the cells can be tetrahedral, pyramidal, hexahedral, or prismatic in shape and formed by several triangular or quadrangular faces A_{il}. The total number of cells is N_{tot}. Let us denote the cell volume as $|\mathrm{Vol}_i|$. Let U_i^n be the average value of the vector of conservative variables in cell i at instant t^n.

The steady-state solution to system of equations (1.1), (1.2) is constructed by the relaxation-in-time method [1], which is not described here. One of the options for constructing a time-implicit scheme for transient problems is to employ the Crank–Nicolson approach, which is used extensively for solving parabolic equations. A symmetric second-order accurate discretization is used within this approach, so for the values of the vector of conservative variables at the upper layer $n + 1$, we have the formula

$$x_j^{n+1} = x_j^n + T_\Omega \Delta t, \quad \frac{U_i^{n+1} - U_i^n}{\Delta t} = \frac{1}{2} R_i\left(U^{n+1}, x^{n+1}\right) + \frac{1}{2} R_i\left(U^n, x^n\right). \tag{1.3}$$

Here, T_Ω is the matrix of rotation around a given axis of the coordinate system. The quantity $R_i(U^n, x^n)$ is an approximation of the differential part of the system and is defined as the sum of numerical fluxes Φ_{li} through the faces of cell Vol_i:

$$R_i\left(U^n, x^n\right) = -\frac{1}{|V_i|}\sum_l \Phi_{li}^n, \quad \Phi_{li} = \int_{A_{li}} \mathbf{n}\mathbf{F}^{ALE} dA, \tag{1.4}$$

where $\mathbf{n} = (n_x, n_y, n_z)^T$ is the outer unit normal to a face.

Piecewise-linear reconstruction with a slope limiter is used to determine the values of the flow variables at the faces of a cell given the cell averaged values of these quantities. The coefficients of the reconstruction polynomial are determined by least–square method in a local coordinate system using the solution values in adjacent cells that enter the so-called reconstruction stencil [4, 5]. The slope limiter is used to suppress possible oscillations of nonphysical nature [6]. The reconstruction procedure performed for each face l of spatial cell i results in a pair of values of conservative variables U^-, U^+. A modification of the HLLC method [7] for a rotating coordinate system [8] is used to determine the convective fluxes.

To determine the solution values at the upper time layer U^{n+1}, it is necessary to solve system of equations (1.4). A straightforward algorithm for finding U^{n+1} in a three-dimensional problem is extremely computationally intensive, requiring an enormous amount of computer memory. It is therefore expedient to take advantage of iterative methods. One of the approaches widely used in industrial codes is integration in so-called pseudotime. Let us introduce a pseudotime $0 \le \tau \le \infty$ and a variable $V(\tau)$ such that

$$\lim_{\tau\to\infty} V_i(\tau) = U_i^{n+1}.$$

We rewrite scheme (1.3) as follows:

$$\frac{d}{d\tau} V_i(\tau) + \frac{V_i(\tau) - U_i^n}{\Delta t} = \frac{1}{2} R_i\left(V(\tau), x^{n+1}\right) + \frac{1}{2} R_i\left(U^n, x^n\right). \tag{1.5}$$

The relevant value of the vector of conservative variables at the upper layer U_i^{n+1} is determined as a steady-state solution to Eq. (1.5) in the pseudo time. For convenience, in what follows, we use the notation

$$V_i^k = V_i(\tau_k), \quad \Delta V_i^k = V_i^{k+1} - V_i^k.$$

Here k is the time step number in pseudo time. By introducing a time discretization with a local step $\Delta\tau_i$,

$$\frac{\Delta V_i^k}{\Delta \tau_i} + \frac{V_i^k + \Delta V_i^k - U_i^n}{\Delta t} = \frac{1}{2} R_i\left(V^k + \Delta V^k, x^{n+1}\right) + \frac{1}{2} R_i\left(U^n, x^n\right),$$

in the discrete form, similar to the steady-state case, we arrive at the following equations for calculating the increment of quantity V_i^k over time:

$$\begin{gathered} D_i \Delta V_i^k + \frac{1}{4|V_i|}\sum_l \left(T_{li}^{-1}\Delta F_{li} - V_{li}\Delta V_{\sigma_l(i)}^k\right)|a_{li}| = \frac{1}{2} R_i\left(V^k, x^{n+1}\right) - \frac{V_i^k}{\Delta t} + Z_i^n, \\ D_i = \left(\frac{1}{\Delta\tau_i} + \frac{1}{\Delta t} + \frac{1}{4|V_i|}\sum_l V_{li}|a_{li}|\right) I, \\ Z_i^n = \left[\frac{1}{2} R_i\left(U^n, x^n\right) + \frac{U_i^n}{\Delta t}\right]. \end{gathered} \tag{1.6}$$

Here, quantities V_{li} are the upper bounds of the eigenvalues of the Jacobian matrix of the numerical flux.

The straightforward solution to linear system of equations (1.6) for increments in the vector of conservative variables is a very complicated problem. In the current paper, the implicit LU-SGS method not involving calculation of Jacobian matrices (the so-called matrix-free method) is used [9]. The procedure for solving the system of linear equations consists of backward and forward sweeps. The backward sweep has the form ($i = N, N-1, \ldots 1$)

$$D_i \Delta V_i^* = -\frac{1}{4|V_i|}\sum_{l:\sigma_l(i)<i}\left(T_{li}^{-1}\Delta F_{li}^* - V_{li}\Delta V_{\sigma_l(i)}^*\right) \times |a_{li}| + \frac{1}{2} R_i(V^k) - \frac{V_i^k}{\Delta t} + S_i^n. \tag{1.7}$$

For the forward sweep we use the relations ($i = 1, 2, \ldots N$)

$$D_i \Delta V_i^k = \Delta V_i^* - \frac{1}{4|V_i|} \times \sum_{l:\sigma_l(i)>i} \left(T_{li}^{-1} \Delta F_{li} - V_{li} \Delta V_{\sigma_l(i)}^k\right)|a_{li}|. \tag{1.8}$$

The criterion for convergence of the inner iterations is that the residual drop by no less than three to four orders of magnitude. The time step Δt^n was calculated by the formula

$$\Delta t^n = K \min_i \frac{h_i}{S_i^n}, \tag{1.9}$$

where S_i^n is an estimate for the maximum (in absolute value) eigenvalue in the cell, K is a prescribed Courant number, and h_i is the characteristic linear dimension of a cell. The explicit scheme corresponds to $K \le 1/3$. Large Courant numbers $K \gg 1$ can be used for the implicit scheme to curtail the solution time.

1.3. Modeling Complexly Shaped Helical Configurations

As mentioned above, numerical simulation of a propeller rotating near a stationary pylon is impossible with only one rotating mesh. In this work, the transition was made to a modeling based on combining the rotating domain (the washer) in the immediate vicinity of an propeller or a pair of propellers and the outer static domain. In other words, the numerical solution is constructed simultaneously on several nonconformal computational meshes, some of which may arbitrarily rotate as a rigid body. Figure 1 shows the typical topology of a multizone computational domain. One can see the rotating washer around the propeller, with the pylon and relevant part of the propeller bushing belonging to the outer static domain. On each of these two meshes, system (1.1) is solved with the domain-specific value of the angular velocity Ω. Nonstationary "joining" of solutions is performed at the shared boundaries.

As a whole, the numerical algorithm for constructing a time-accurate transient solution operates as follows. At the initial instant, the flow field is initialized with values obtained from the steady-state calculation. On passing from moment t^n to moment t^{n+1}, the solution is found in each of the computational domains with algorithm (1.6), which involves rotation of the mesh in the washer. When this happens, information on the connectivity of cells bordering the boundary on each side is updated on every sliding plane between the zones. Data exchange on the sliding domain boundaries and interpolation of the values of the vector of conservative variables occur in the course of pseudotime iterations. The solution to the problem is thus approximated both spatially and temporally in several nonconformal domains.

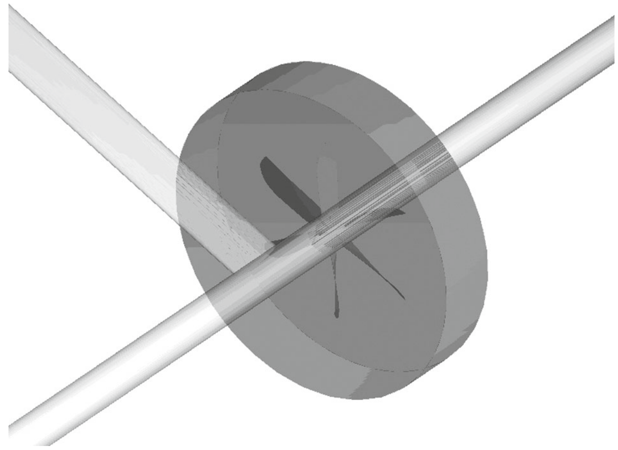

Fig. 1. Topology of computational domain for simulating the discussed six-bladed propeller with pylon.

Switching to multizone computational meshes necessitated changes to the algorithm for computing convective fluxes near the boundary between rotating blocks, as well as modifications to the implicit LU-SGS algorithm near the block boundary, to improve the algorithm's reliability.

In this work, we use a numerical technique that does not rely on the assumed conformality of the vertices of meshes from different zones. In this approach, for every boundary cell i_K from a given zone K, we find a boundary cell $j_M(i_K)$ from zone M that is closest to the face l of the former cell; the latter cell touches the common boundary with its face with number l_1.

The algorithm for calculating numerical fluxes uses information on the solution from cells i_K and $j_M(i)$ and their neighbors in order to calculate the values of

$$\Phi_{li_K} \equiv \Phi_{l_1 j_M}. \tag{1.10}$$

In the greater part of the flow, the numerical technique uses an algorithm for constructing the reconstruction polynomial, based on the least squares method. The stencil-construction algorithm adds the required number of neighbors to cell V_i. However, the construction of such a stencil is complicated for cells near the boundary with another cell zone (domain), because one or several cell faces may not have an immediate neighbor. A very complex procedure of copying data from the neighboring zone needs to be implemented for the least-squares method to be used, especially when the solution is carried out on parallel computers.

In this study, the least squares method is supplemented with a procedure for calculating the coefficients of a piecewise-linear approximation of the solution in cells using the divergence (Gauss–Ostrogradsky) theorem. For a cell V_i for which all its neighbors belong to the same mesh zone, the gradient of the scalar function f is estimated as follows:

$$\nabla f \approx \frac{1}{|V_i|}\sum_l n_l f_{li}|A_{li}|, \tag{1.11}$$

where n_l is the outer unit normal to face l and f_{li} is the approximate value of f on this face, which is equal to the arithmetic mean between f_i and the value in the adjacent cell with index $\sigma_l(i)$. After this, the values on every cell face V_i are calculated by the simple formula

$$f^- = f_i + \nabla f\left(x_{\text{face}} - x_{\text{cell}}\right). \tag{1.12}$$

Formula (1.12) can easily be generalized to include cells near the boundaries between zones. If a face l belongs to the boundary between zones, then instead of the nonexistent value from cell $\sigma_l(i)$, the value from the closest cell of a neighboring (bordering) zone with number $j_M(i)$ is used. As a result, the calculation of face values makes use of the values of unknowns in the cells from both adjoining zones; the gradient formula itself is centered around cell V_i rather than one-sided.

Let us describe a modification of the LU-SGS algorithm on sliding planes. First, it should be noted that the direct and inverse steps in the method are cycles with explicit data dependence. This leads to difficulties at the boundaries between zones, especially in parallel computing. The simplest way to avoid this constraint is to ignore values in cells from the neighboring zone. The advantage of this method is its simplicity, i.e., the LU-SGS procedure also requires additional verification that the neighboring cell belongs to this zone and, once this has been done, every mesh zone can be processed independently of the others. The drawback, though, is that the procedure for determining the increments of the solution breaks down into several unconnected domain traversals. For solutions with a complex vortex structure, this may bring down the reliability of computing in pseudotime iterations and deteriorate the convergence rate.

It this work, it is proposed to treat cells that belong to another zone as fictitious and to use the Jacobi approximation in them:

$$\Delta V_i^k = \frac{1}{D_i}\left(\frac{1}{2}R_i\left(V^k, x^{n+1}\right) - \frac{V_i^k}{\Delta t} + Z_i^n\right). \tag{1.13}$$

This idea is similar to the approach used earlier in literature for multithreaded realization of the LU-SGS method [10].

2. PARALLEL SOFTWARE PACKAGE

The above numerical techniques were implemented in an aeroacoustic parallel software package. This software package is distinct in that it can simulate a transient flow of compressible gason advanced supercomputers for complex configurations with rotating parts, such as rotor–pylon, two rotors–pylon–wing, etc. The original software source code was created using Fortran 2008.

2.1. General Description of the Software Package Architecture

The current software version uses an object-oriented hierarchical model of classes (structures). The first level comprises the structures that describe the computational mesh components (vertex, face, cell) as well as the mesh as a whole. The encapsulated procedures for these structures make it possible to read the computational mesh in the StarCD and Gambit formats; construct vertex–cell, vertex–face, and face–cell connectivity graphs; determine face areas and cell volumes; etc. The second level includes the class Problem, which corresponds to construction of a solution on a single-zone mesh and includes the class Mesh. Procedures for computing physical quantities, numerical fluxes, and the LU-SGS method are implemented within the class Problem.

Finally, a container class is implemented at the third level and includes an arbitrary number of instances of the class Problem. The main procedure in the container is a parallel algorithm for interpolating data at the boundaries of different domains. An additional class Surface makes it possible to interpolate design data to an arbitrary number of fixed surfaces of the Ffowcs Williams–Hawkings method (FWH surfaces). Several FWH surfaces were, as a rule, used in calculations to check the sensitivity of the noise calculation result to the parameters of these surfaces.

2.2. Organization of Parallel Computing

To run supercomputer calculations, the software package has a hybrid two-level MPI+OpenMP computing model, which has been actively developed in recent years as applied to gasdynamic and kinetic calculations [11, 12]. In this model, the OpenMP technology is used within one cluster node, while exchange between the nodes is performed with MPI.

From the viewpoint of parallel computing, the complicated part of the software is its parallel algorithm for interpolating data on sliding planes between zones, e.g., between the rotating mesh around the propeller and the static mesh around the pylon. The presence of sliding boundaries is known to be a serious problem in ensuring good parallel scalability of software. In this study, every MPI process stores the entire set of coordinates of faces on both sides of the sliding boundary. After mesh rotation at the beginning of a time step, for a part of the sliding surface belonging to the current MPI process, a parallel multithreaded OpenMP algorithm of search for neighbors that are adjoining on the other side of the sliding boundary is used.

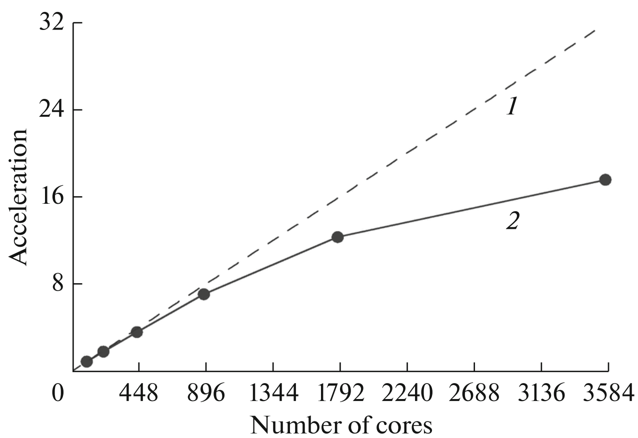

Fig. 2. Testing of scalability of software package on Politekhnik RSK Tornado cluster with use of 4 to 128 nodes (112–3584 cores): (*1*) ideal scaling, (*2*) calculation.

Test calculations were performed using the Lomonosov-2 supercomputer of Moscow State University [13] under the project Supercomputer Potential of Russian Industry, as well as the RSK Tornado supercomputer of Peter the Great St. Petersburg Polytechnic University. For example, Fig. 2 shows the results of testing the two-level OpenMP + MPI algorithm on RSK Tornado cluster on a two-zone tetrahedral computational mesh (washer + surrounding space) consisting of 3 million cells. From 4 to 128 cluster nodes (112–3584 physical cores) were used. It can be seen that, despite using a computational meshes with a relatively small number of cells, the software package adequately scales up as the number of used system nodes increases.

The RSK Tornado system at the Supercomputer Simulation Laboratory (SSL) of South Ural State University was used to run the main calculations. Satisfactory scalability was achieved with this system with up to 100 cluster nodes, a figure that corresponds to 1200 physical Inter Xeon cores (2400 hyperthreads).

3. COMPUTATIONAL MODES, MESHES, ORGANIZATION OF PARALLEL COMPUTING, AND CALCULATION TIME

The developed software package was used in this work to study the effect of propeller mounting (puller or pusher assembly) on the environmental noise of advanced aircraft. For this purpose, based on a model six-bladed propeller [1] with a blade angle of 50° and a radius of 15 cm, two geometrical configurations with a pylon were created:

(1) a propeller with a pylon in front of it (pusher scheme), Fig. 3a;

(2) a propeller with a pylon behind it (puller scheme), Fig. 3b.

In the calculations, a flow regime with the free-stream velocity $u_z = -40$ m/s and a propeller speed of 7740 rpm was used.

For each configuration, two-zone computational spatial meshes were created that comprised a rotating washer around the propeller and a fixed mesh in the remaining part of the domain, as well as several test FWH surfaces with the parameters listed below.

A series of calculations were performed in this study in order to determine the optimum computational mesh parameters, such as the domain size and refinement toward the surface of the propeller, pylon, and washer boundary.

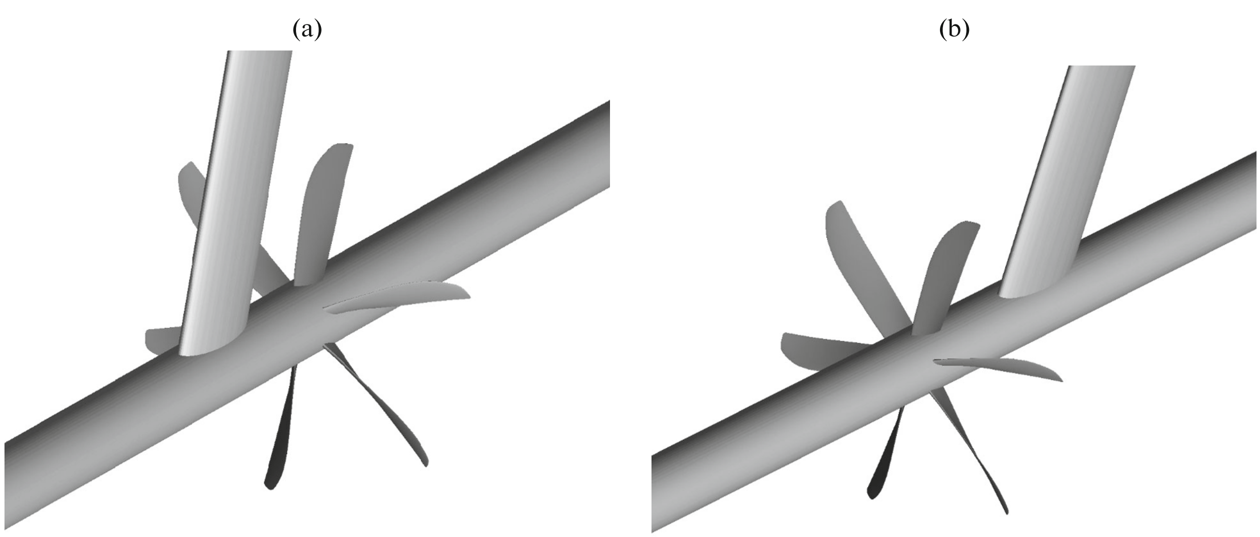

Fig. 3. Problem geometry: (a) pylon in front of propeller (pusher scheme), (b) pylon behind propeller (puller scheme).

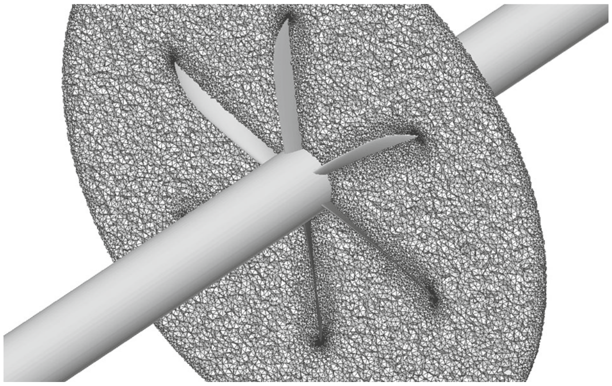

Fig. 4. Tetrahedral mesh in washer with 6.4 million tetrahedra.

The longitudinal size of the washer is determined by the proximity of the propeller and pylon mounting; the washer diameter was 250 mm. The cell size was 2 mm on blade surfaces, 4 mm inside the washer, and 3 mm on the washer surface. These mesh parameters were selected based on the condition of having sufficient resolution for propeller-geometry elements as well as constraints imposed by the computational cluster available to the authors. The section of the computational mesh for the washer is shown by the transverse plane in Fig. 4.

For the outer (static) part of the computational domain, it was established that the boundary of the outer domain should be at least 10 m away from the propeller, otherwise reflections from the boundaries significantly affect the acoustic field inside the domain. The total number of cells inside the washer was 6.4 million; in the outer domain, 13 million. The section of the computational mesh by the symmetry plane in the static domain is shown in Fig. 5.

In addition to the above, a steady-state solution to the problem for an isolated propeller was constructed to verify the noise calculations by the method explained in [1]. The computational mesh parameters and the domain size were taken the same as for the transient problem.

It should also be noted that the transient flow was typically calculated until a physical time instant equivalent to ten propeller revolutions; it took 24 h of computer time for 96 cluster nodes at South Ural State University.

4. CALCULATING PROPELLER NOISE

4.1. Noise Calculation Procedure and Its Verification

In the code being developed, far-field noise was calculated using the Ffowcs Williams–Hawkings (FWH) method with the convective Green's function [14], since the presence of a free-stream flow (imitation of aircraft in flight) had to be taken into account.

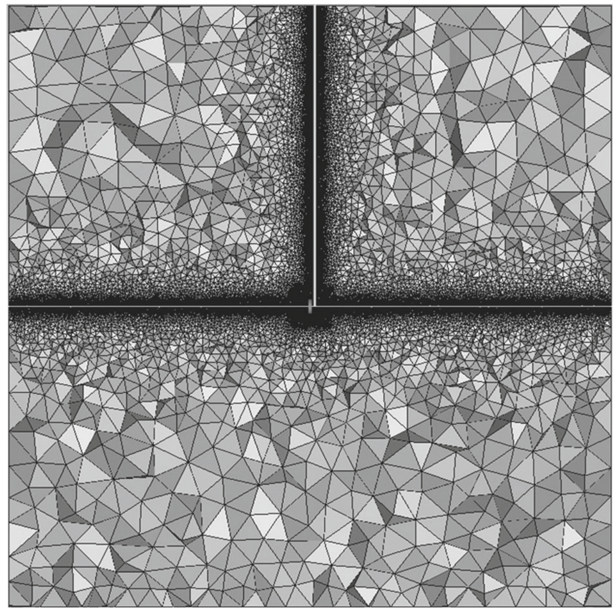

Fig. 5. Tetrahedral mesh condensing toward pylon and washer in outer domain with 13 million tetrahedra.

In this work, the FWH noise calculation software, originally used to calculate jet noise [15], was adapted to fit the data output format employed in the software for calculating a transient flow past a propeller. The following two steps are performed to obtain a far-field sound signal from transient calculation results, with each step being verified to avoid noise calculation errors:

(1) interpolation of transient solution data from the computational domain cells to the cells of a test FWH surface;

(2) extrapolation of data from an FWH surface to the far field.

The test problem of calculating noise from a point dipole in a medium at rest was formulated for verification. Given such a noise source, all hydrodynamic quantities can be calculated analytically. A dipole oriented along the z axis was considered (Fig. 6a). Dipole parameters were selected so that the frequency corresponded to typical values obtained at the blade passing frequency when testing small-scale propellers: $f = \omega/(2\pi) = 500$ Hz (e.g., a six-bladed propeller with 5000 rpm).

A dipole-encompassing cylinder with the symmetry axis along the z axis was taken as the FWH surface. The FWH surface dimensions were chosen approximately the same as for calculating propeller noise (see the following section), with the fineness of partitioning selected at ~0.05 m (Fig. 6b), a value on the verge of the resolving power for the relevant wavelength (0.67 m). This was done to estimate typical noise calculation errors due to the finiteness of the dimensions of cells on the FWH surface. With the same purpose of

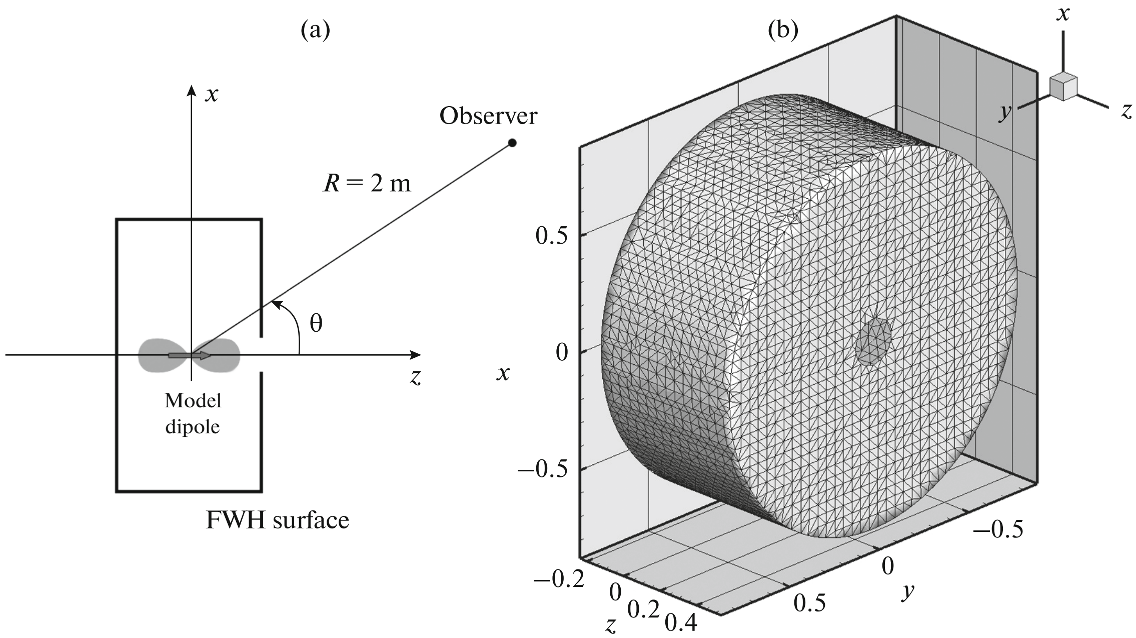

Fig. 6. Verification of noise calculation procedure: (a) model problem formulation, (b) FWH surface split into cells.

assessing calculation errors, a circular hole 0.2 m in diameter was cut on one of the FWH butt-end surfaces, a value close to the propeller diameter. Since the model dipole is oriented along the axis of the cylindrical FWH surface, i.e., the maximum of its emission falls precisely on the area of the center of the butt-end surfaces, the presence of the circular cutout at the center of the FWH surface may distort the signal in the far field. This test problem thus makes it possible to verify the procedure of extrapolating noise from the FWH surface and assess from above the errors in such extrapolation for the most unfavorable parameters (a coarse mesh on the FWH surface and the presence of cutouts in it).

To verify the procedure of interpolating from the computational mesh cells to FWH surface cells, the noise from the FWH surface to the far field was calculated in two ways. Analytical expressions were used as the FWH surface data in the first case, while in the second case, analytical expressions were used to derive the values on the spatial computational mesh, with the values on the FWH surface being obtained by interpolation of the former values to the FWH cells.

Calculations were performed for 13 observation points located in the xOz plane on an arc with a radius of 2 m and a pitch of 15° for a range of polar angles θ of 0°–180° (counted from the z axis). The calculation results are shown in Fig. 7. The FWH calculations (for the two cases with and without interpolation) were compared with the analytical solution.

The results demonstrate good agreement between calculation and the analytical solution in the domain $z < 0$. The agreement is significantly poorer (a discrepancy of 1 dB) in the domain $z > 0$. This is explained by the cutout in the butt-end FWH surface for $z > 0$ in the area of the dipole's strongest emission. Note that the agreement between calculations with and without interpolation is really good (with a discrepancy of no more than 0.4 dB), which indicates the validity of the interpolation procedure even on such a coarse mesh.

The examination of the model problem has thus shown that the procedure for calculating far-field noise based on the time-dependent field of pulsations on an FWH surface works correctly and can be used to calculate propeller noise.

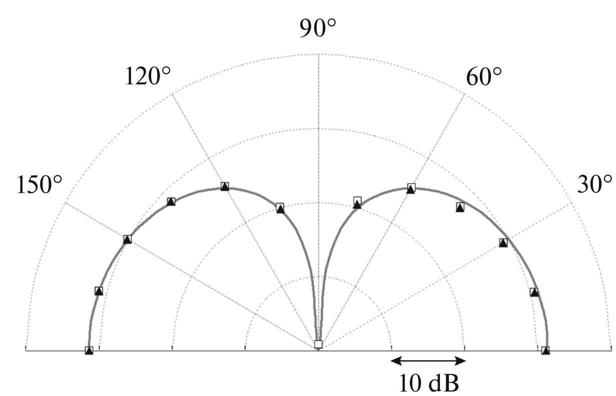

Fig. 7. Dipole emission directivity pattern. Comparison of FWH calculation with analytical solution: line is exact solution, ▲ is FWH calculation with interpolation, □ is FWH calculation without interpolation.

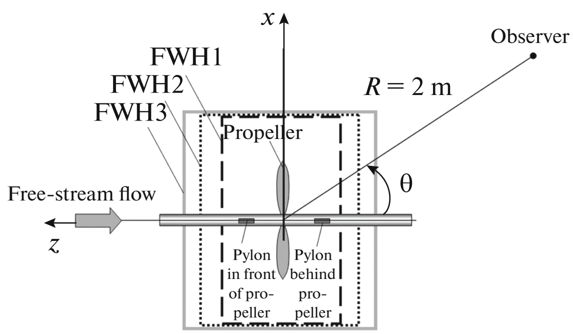

Fig. 8. Sketch of configuration for calculating noise from isolated propeller in puller and pusher configurations.

4.2. Calculating Propeller Noise in the Puller and Pusher Assemblies

One of the main goals of this article was to work through the procedure of calculating far-field noise produced by a propeller (in different assemblies) based on the results of transient calculations, since pylon assemblies can be correctly compared and birotating propellers can be considered only in the framework of transient calculations.

Noise was calculated using the FWH method and verified (as applied to the specific features of the software for calculating aerodynamic characteristics) in the previous section. Far-field noise was calculated using three cylindrical FWH surfaces (FWH1, FWH2, FWH3) with the axis coinciding with the z axis (and the propeller rotation axis), the same base diameter of 0.5 m, and different heights (generatrix lengths) of 0.8, 0.9, and 1.0 m. The surfaces were symmetrical with respect to the coordinate origin. Noise was calculated at 13 observation points located in the xOz plane (perpendicular to the pylon) on a circular arc with a radius of 2 m and a pitch of 15° for a range of polar angles $\theta = 0°-180°$ (counted from the direction of the free-stream flow). A sketch of this configuration is shown in Fig. 8.

Several FWH surfaces are required in order to check the sensitivity of the produced sound signal to the position and size of the surface. In noise calculations, it is necessary to find a computational domain zone in which the sensitivity of the acoustic signal to the FWH surface parameters is small. Ideally, when the FWH surface is in a domain in which the wave equation holds true, the noise calculation result should not depend on the surface parameters at all. However, in actual problems, noise calculation can be affected by the specific features of the computational mesh as well as by surface perturbations of a nonacoustic nature. For example, placement of the surface too far from the source in a domain of a highly spaced mesh may lead to understated high-frequency pulsations. At the same time, vortex perturbations on the test surface may lead to overstated noise. However, since the convection of such perturbations occurs with a speed that is approximately equal to the local flow velocity, which is significantly different from the speed of sound, the phases of the contributions from these perturbations to the acoustic pressure at any far-field point are, generally speaking, different for different surfaces. Meanwhile, sound waves intersecting the FWH surfaces propagate at the speed of sound and the phases of the corresponding contributions to the far-field acoustic pressure coincide so that the “true” signal is not distorted after averaging over FWH surfaces. This effect can therefore be attenuated by averaging over several surfaces [16].

Comparison of calculations for computational domains of different sizes—2, 10, and, 25 m—showed that in all cases, the noise spectra exhibit a tone component at the blade passing frequency; however, whereas the peak values for the 10 and 25 m domains are very close, the peak for the small domain is overstated by 4 dB, which in all likelihood is directly related to the proximity of the computational domain boundaries to the propeller. Based on the results of this testing, 10 m computational domains were used in all subsequent calculations.

Let us consider how the result is affected by the choice of the FWH surface. Figure 9 shows the results of spectral processing of far-field signals over three FWH surfaces for one of the observation points, at 90° to the propeller axis (the observer is in the propeller disk plane). The noise emission maximum at the blade passing frequency is usually observed close to this direction. The blade passing frequency (BPF1) can be clearly seen, as is usually the case for propeller noise for a favorable flow regime (on the one hand, there is noticeable thrust, but on the other hand, the blade’s local angles of attack are not too high, with the flow past the blades remaining attached). Several lower-amplitude harmonics of the blade passing frequency can also be seen (BPF2, BPF3). The magnitude of the BPF1 peak does not depend on the choice of the FWH surface, as should be the case given correct calculation and choice of test surface; in addition, the broadband noise level is also approximately the same for all surfaces.

The energy contained in the BPF1 peak is approximately 60% of the total signal energy (for $\theta = 90°$). The remaining energy is mainly related to rather powerful broadband noise, which should be considered nonphysical in calculations based on the Euler equations, since they do not correctly describe the non-steady-state generation of vortex structures and the corresponding field of turbulent pulsations. At the same time, it is known [18] that the levels of spectral peaks at the blade passing frequency and its harmonics are determined by steady-state (with regard to the blades) parameters, including mean forces and moments acting on the propeller. Hence, since the Euler equations for describing flow past propellers yields acceptable accuracy in calculating such average parameters, this implies that the tone propeller noise components (at the BPF1 frequency and its harmonics) are described quite correctly, provided, of course, that their level is sufficiently high compared to the broadband noise level.

Figure 10 shows the pulsation spectra for different observation angles. In the case at hand, it can be concluded that the BPF1 peak (its magnitude) has physical meaning because it is above the broadband noise level by more than 10 dB for angles of observation of 30°–150°. This suffices to estimate propeller noise in the main approximation, because it is this peak that is prevalent in experimental research. The main attention will be devoted to analyzing noise characteristics specifically at the BPF1 frequency. All directivity patterns will be constructed in what follows for angles θ = 30°–150°.

It should also be noted that so-called phase averaging [17] is often used in actual propeller noise measurements, a technique that makes it possible to isolate tone components in a more explicit way against the broadband noise background. This technique, however, was not utilized in the current research because, as will be shown, the fundamental harmonic significantly exceeded the background noise level for virtually all viewing angles. Moreover, applying phase averaging to numerical simulation is cumbersome, because it involves calculations for a large number of propeller rotations, thus placing a significant demand on computational resources.

Figure 11 compares the directivities at the fundamental harmonic in the puller assembly obtained using the three test surfaces indicated above. It can be seen that the results are rather close (to within ±1.5 dB) in the entire range of angles of observation where the fundamental harmonic manifests itself explicitly. In what follows, the results obtained from the FWH1 surface are used.

Figure 12 compares the noise spectra in the puller and pusher assemblies at the BPF1 frequency. The presence of a pylon can be seen to deform the directivity pattern. Putting the pylon in front of the propeller increases noise in the forward hemisphere and, vice versa, the pylon behind the propeller causes more noise to be emitted in the aft hemisphere. These effects may be related to the interference between the primary (propeller) and secondary (pylon) noise sources.

4.3. Separation of the Propeller and Pylon Contributions to the Total Noise

Merely adding up the emission spectra of the propeller itself and a signal due to reflections from airframe elements is not sufficient to account for the effect of mounting in noise calculations. This approach would have been correct only if these sources were uncorrelated. In reality, acoustic signals

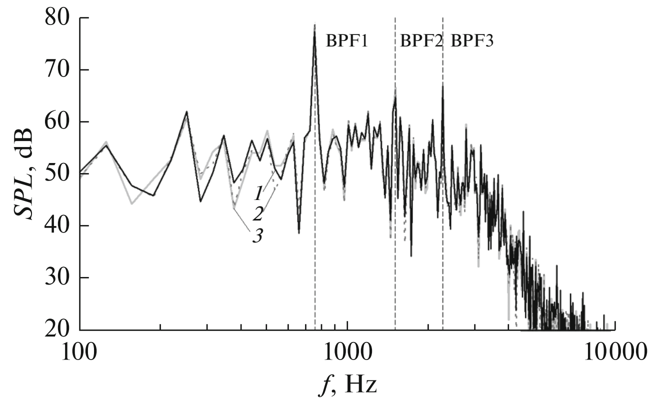

Fig. 9. Comparison of far-field noise spectra (θ = 90°) obtained using different control FWH surfaces: (*1*) FWH1, (*2*) FWH2, (*3*) FWH3. The vertical lines indicate the blade passing frequency and its harmonics.

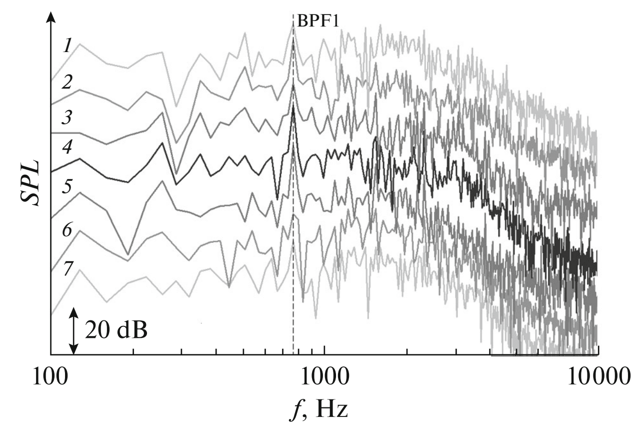

Fig. 10. FWH1 surface propeller noise spectra for different polar angles: (*1*) $\theta = 0°$, (*2*) 30°, (*3*) 60°, (*4*) 90°, (*5*) 120°, (*6*) 150°, (*7*) 180°. For convenience, every subsequent spectrum is shifted by 15 dB with respect to the previous one.

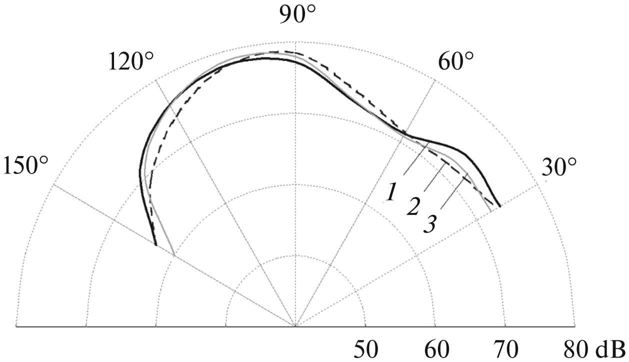

Fig. 11. Comparison of directivities of fundamental harmonic of puller configuration obtained using different control surfaces: (*1*) FWH1, (*2*) FWH1, (*3*) FWH3.

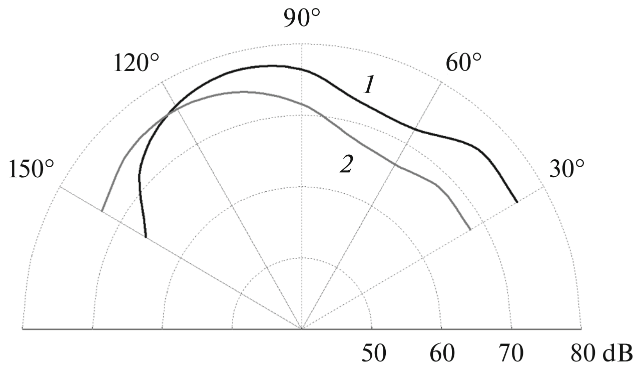

Fig. 12. Comparison of directivities of fundamental harmonic for (*1*) puller and (*2*) pusher configurations.

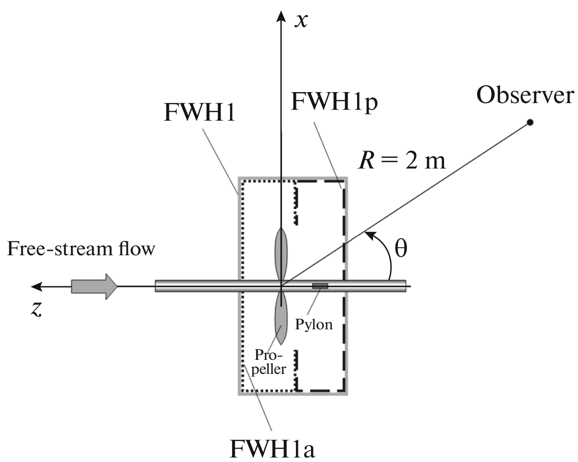

Fig. 13. Sketch of FWH surfaces in puller configuration for separating contributions of propeller and pylon to total noise.

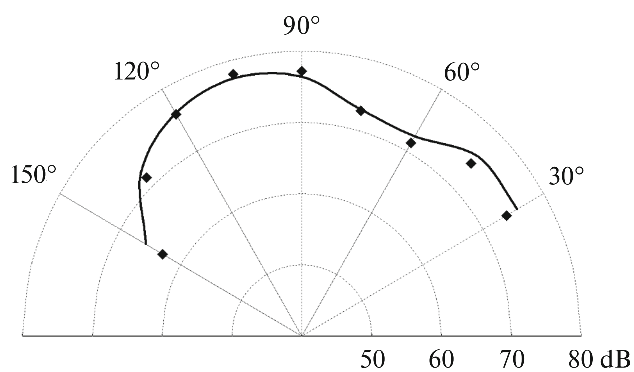

Fig. 14. Comparison of noise directivities for the sum of acoustic signals (line) from propeller (FWH1a) and pylon (FWH1p) and for signal emitted from FWH1 surface comprising propeller and pylon (symbols).

emitted by the propeller and mounting elements at the BPF1 frequency are phased, and their interference needs, therefore, to be taken into account in the overall noise assessment.

In this study, interference between propeller- and pylon-related sound signals was studied for the more common puller configuration (the pylon is downstream of the propeller). To this end, two additional test surfaces, formed on the basis of the FWH1 surface, were used in sound emission calculations. The FWH1a surface covered only the propeller, with the FWH1p surface enveloping the pylon. The extents of the surfaces in the axial direction were as follows:

$-0.4 < z < 0.4$ m for FWH1;

$-0.075 < z < 0.4$ m for FWH1a;

$-0.4 < z < -0.075$ m for FWH1p.

Cutouts with a radius of 0.2 m (Fig. 13) were made in the FWH1a and FWH1p surfaces at $z = -0.075$ (the propeller wake here was the most intensive). As shown in the test problem with a dipole, such a modification has a relatively small effect on the accuracy of sound field calculations while eliminating the nonphysical contribution of the propeller's vortex wake to the acoustic signal.

First of all, the computed far-field directivities of the fundamental noise harmonic were compared for a signal emitted from the FWH1 surface and for the sum of signals emitted from the FWH1a and FWH1p surfaces (Fig. 14). It can be seen that the noise directivities calculated by these two methods are close; i.e., the error associated with difference in the interpolation of solutions at the FWH surface is negligibly small.

This creates the possibility of isolating the contributions of emission by the propeller itself and emission due to the presence of a pylon to the total noise. Figure 15 shows the directivities of emissions of these two noise components at the fundamental harmonic. In particular, it can be seen from this figure that, given the small angles with the propeller axis, the total noise proves lower than one of its components due to interference between signals from the propeller and pylon.

The FWH1a surface signal, which is the contribution of the propeller noise, was verified by its comparison with the calculation results for the noise from an isolated propeller based on the steady-state distribution of parameters on the blades (Fig. 15). It can be seen that the calculation results agree with each other to within 2 dB near the emission maximum (45°–135°), which indicates correct operation of the nonstationary solver.

The influence of interference on noise can be seen in Fig. 16, which compares the directivities of the fundamental harmonic for the sum of the propeller and pylon signal powers, which does not allow these signals to be phased, with the total signal from the propeller and pylon, which correctly takes into account the interference between these two sources. It follows from the figure that the effect of interference can be either positive or negative.

The interference effect can be illustrated with the following simple example. Suppose we have two sig-

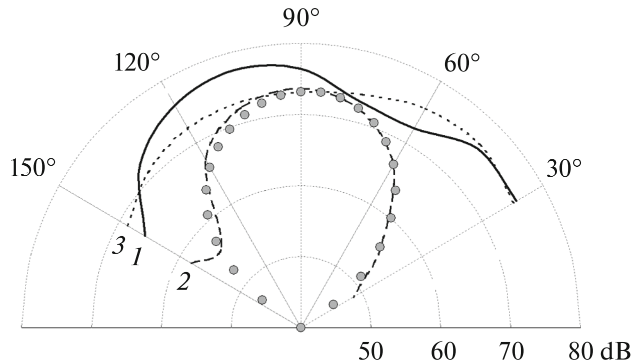

Fig. 15. Directivity pattern for noise components related to propeller and pylon: (*1*) total noise as signal emitted from FWH1 surface; (*2*) propeller noise as signal emitted from FWH1a surface, (*3*) pylon noise as signal emitted from FWH1p surface. Symbols indicate directivity pattern of propeller noise obtained from steady-state calculation without pylon.

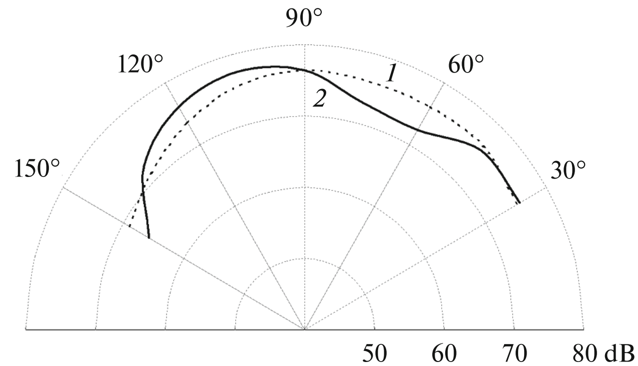

Fig. 16. Comparison of the sum of propeller and pylon signals without (sum of powers, curve (*1*)) and with (sum of signals, curve (*2*)) allowance for interference.

nals that have the same amplitude but are phase-shifted, i.e.,

$$p_1(t) = A\cos\omega t, \quad p_2(t) = A\cos(\omega t + \varphi).$$

The power of each signal is

$$N_1 = N_2 = \frac{1}{T}\int_0^T p_1^2(t)\,dt = \frac{1}{2}A^2, \quad T = \frac{2\pi}{\omega}.$$

Summation of these powers yields $N_1 + N_2 = A^2$. At the same time, the total signal power is

$$N_{1+2} = \frac{1}{T}\int_0^T (p_1(t) + p_2(t))^2 dt$$
$$= \frac{1}{T}\int_0^T A^2\left[\cos^2\omega t + \cos^2(\omega t + \varphi)\right.$$
$$\left. + \cos(2\omega t + \varphi) + \cos\varphi\right]dt = A^2(1 + \cos\varphi).$$

Thus, summation of the powers of the two signals may result, depending on the phase shift φ, in a value that may be either higher or lower than the composite signal power. The maximum positive effect of the interference is achieved for the phase shift of $\varphi = \pi$, when the two equal-power signals are in antiphase and completely cancel each other. On the contrary, the negative effect of the interference takes place when the signals are in-phase, i.e., $\varphi = 0$. In this case, the composite signal power is double the power it would have been for uncorrelated signals.

It can be seen from the plot in Fig. 16 that the total signal power exceeds the sum of the powers of the individual signals at an angle of 105° to the propeller axis, $N_{12} > N_1 + N_2$, while in the direction 60° from the propeller axis, by contrast, it falls below it, i.e., $N_{12} < N_1 + N_2$. Based on the above analysis, it can be expected that the propeller- and pylon-related sound signals are in-phase in the direction 105° and, on the contrary, in antiphase in the direction 60°. Indeed, the time histories of the signals (Figs. 17 and 18) support this conclusion and demonstrate correspondence between the phase shift of the propeller and pylon signals and the effect of amplification or attenuation of the total noise due to interference.

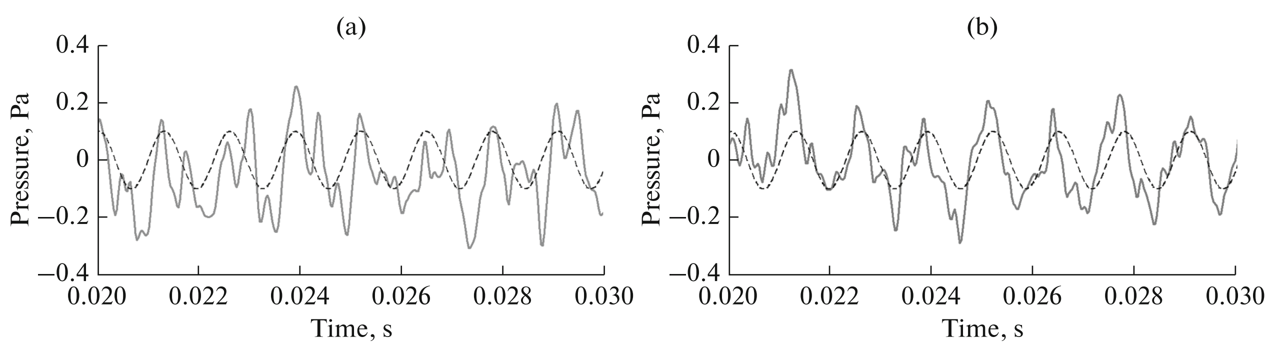

Fig. 17. Determination of phase of fundamental harmonic of signals from (a) propeller and (b) pylon at angle of 105° to propeller axis. Solid lines denote total signal; dashed lines, fundamental harmonic.

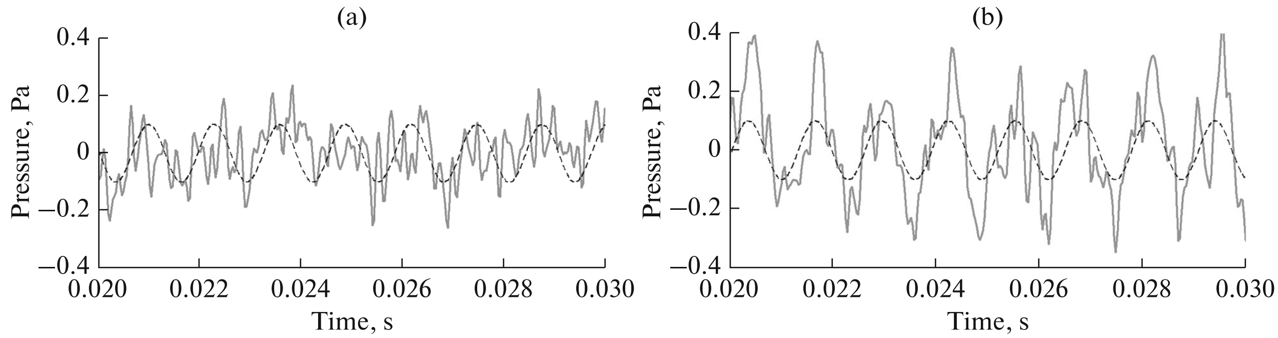

Fig. 18. Determination of phase of fundamental harmonic of signals from (a) propeller and (b) pylon at angle of 60° to propeller axis. Solid lines denote total signal; dashed lines, fundamental harmonic.

The effect of propeller sound emission interfering with a signal from the propeller-mounting elements can be either positive or negative as far as noise is concerned. One can, therefore, state the problem of optimizing the design of an aircraft with the aim of its noise reduction by varying the geometrical propeller-mounting parameters so as to reduce emission in the direction of certified control points by making use of interference.

CONCLUSIONS

A parallel software package has been developed for solving time-dependent aerodynamics equations. The software makes it possible to predict noise of propellers with complex configurations having rotating parts, such as rotor–pylon, two rotors–pylon–wing, etc. An implicit second-order numerical method on unstructured meshes has been implemented in the package. The method includes a time-accurate algorithm for approximating convective fluxes on sliding planes between different mesh domains and an MPI+OpenMP two-level parallel model.

The software package was used to study the influence of propeller mounting (puller or pusher scheme) on the tonal far-field noise component. Two geometrical configurations were created to this end based on a model six-bladed propeller, i.e., the puller configuration, with a pylon installed in front of the propeller, and the pusher configuration, with a pylon behind the propeller. In the non-steady-state case, a noise calculation procedure by the integral Ffowcs Williams–Hawkings method has been realized with the use of the Green's function for the convective wave equation, making it possible to properly account for the free-stream flow.

It has been shown that propeller noise at the emission maximum (in and near the propeller plane) is dominated by a tonal signal at the blade passing frequency, which is consistent with the known experimental and theoretical data. Based on the nonstationary calculation performed for a model propeller, the influence of the pylon position (puller or pusher configuration) on the characteristics of the fundamental harmonic of propeller noise has been studied. It has been shown than in the pusher configuration, noise amplification is observed in the forward hemisphere, while in the puller configuration, on the contrary, more noise is emitted in the aft hemisphere.

Interaction between noise sources in the propeller–pylon system has been analyzed for the puller configuration. Propeller- and pylon-related components have been separated in the overall noise. The thus-obtained propeller-noise directivity pattern has been compared with noise calculation results based on loads on the blades of an isolated propeller, and the two were shown to agree. It has been demonstrated that when estimating the overall noise generated by the propeller–pylon system, if it is assumed that the sources are uncorrelated, this may lead to a substantial error, with the interference between propeller sound emission and a signal from the pylon (and other airframe elements) capable of producing either a positive or negative effect.

Thus, once properly taken into account, the interference effect can be used to optimize the aircraft design with the aim of reducing environmental noise. It should be noted that the significance of the above interference effect for actual configurations will depend on the relationship between the contributions to the overall propeller noise from the harmonic and broadband components, which in turn depend on the blade geometry, the regime of the flow past them, etc. Numerical simulation of the broadband propeller noise component is a significantly more complicated problem compared with calculation of the tone components; it is related to the necessity of being able to resolve rather fine vortices, a task that would require even more significant computational resources and massive computational meshes. In the future, the authors plan to implement such methods as applied to propeller noise.

ACKNOWLEDGMENTS

The authors are grateful to I.V. Belyaev for his help with the acoustic processing of steady-state calculations. The research has been carried out using the equipment of the shared research facilities of HPC computing resources at Lomonosov Moscow State University [13] and partially supported by a grant from the RF government pursuant to Decree no. 220 "On Measures to Attract Leading Scientists to Russian Higher Professional Education Institutions," agreement no. 14.Z50.31.0032. The part of the study related to calculating single propeller noise for steady blade loads was carried out under the State Assignment of the Ministry of Education and Science of the Russian Federation (no. 9.1577.2017/4.6).

REFERENCES

1. I. V. Belyaev, V. F. Kopiev, and V. A. Titarev, Uch. Zap. TsAGI **45** (2), 78 (2014).
2. A. J. Gil, J. Bonet, J. Silla, and O. Hassan, Int. J. Numer. Methods Biomed. Eng., No. 26, 770 (2010).
3. R. Sevilla, A. J. Gil, and M. Weberstadt, Comput. Struct., No. 181, 89 (2017).
4. M. Dumbser and M. Kaser, J. Comput. Phys. **221** (2), 693 (2007).
5. M. Dumbser, M. Kaser, V. A. Titarev, and E. F. Toro, J. Comput. Phys. **226**, 204 (2007).
6. V. Venkatakrishnan, in *Proc. 31st Aerospace Science Meeting and Exhibit* (Reno, NV, January 11–14, 1993), Paper No. AIAA 93-0880.
7. E. F. Toro, *Riemann Solvers and Numerical Methods for Fluid Dynamics,* 3rd ed. (Springer, 2009).
8. H. van der Ven and J. J. W. van der Vegt, J. Comput. Phys. **191** (41–42), 4747 (2002).
9. I. S. Men'shov and Y. Nakamura, in *Proc. 6th Int. Symposium on CFD* (Lake Tahoe, NV, 1995), Vol. 2, p. 815.
10. A. M. Wissink, A. S. Lyrintzis, and R. C. Strawn, AIAA J. **34** (11), 2276 (1996).
11. I. V. Abalakin, P. A. Bakhvalov, A. V. Gorobets, A. P. Duben', and T. K. Kozubskaya, Vychisl. Metody Program. **13** (3), 110 (2012).
12. V. A. Titarev, S. V. Utyuzhnikov, and A. V. Chikitkin, Comput. Math. Math. Phys. **56** (11), 1919 (2016).
13. Vl. V. Voevodin, S. A. Zhumatii, S. I. Sobolev, A. S. Antonov, P. A. Bryzgalov, D. A. Nikitenko, K. S. Stefanov, and Vad. V. Voevodin, Otkrytye Sist., No. 7, 36 (2012).
14. A. Najafi-Yazdi, G. A. Bres, and L. Mongeau, Proc. R. Soc. A **467**, 144 (2011).
15. G. A. Faranosov, V. M. Goloviznin, S. A. Karabasov, V. G. Kondakov, V. F. Kopiev, and M. A. Zaitsev, Comput. Fluids **88**, 165 (2013).
16. M. L. Shur, P. R. Spalart, and M. Kh. Strelets, Int. J. Aeroacoust. **4** (3–4), 213 (2005).
17. V. F. Kop'ev, M. Yu. Zaitsev, N. N. Ostrikov, S. L. Denisov, S. Yu. Makashov, V. A. Anikin, and V. V. Gromov, Acoust. Phys. **62** (6), 741 (2016).
18. B. Magliozzi, in *Aeroacoustics of Flight Vehicles: Theory and Practice,* Vol. 1: *Noise Sources,* Ed. by H. Hubbard (NASA Langley Research Center, Hampton, VA, 1991), p. 1.

Translated by V. Potapchouck